Polymeric coating lubricates nanocontainers to escape macrophage uptake for bioreceptor recognition

Yulong Sun [a,e,f,1], Yanxin Han [b,1], Yannong Dou [c], Xinqi Gong [d], Haimang Wang [a], Xiaoyu Yu [e], Qiang Wang [a], Yixin Wang [a], Yue Dai [c], Fangfu Ye [e,f], Wei Jin [b,*], Hongyu Zhang [a,**]

[a] *State Key Laboratory of Tribology, Department of Mechanical Engineering, Tsinghua University, Beijing, 100084, China*
[b] *Department of Cardiovascular Medicine, Heart Failure Center, Ruijin Hospital, Shanghai Jiao Tong University School of Medicine, Shanghai, 200025, China*
[c] *Department of Pharmacology of Chinese Materia Medica, China Pharmaceutical University, Nanjing, 210009, China*
[d] *Institute for Mathematical Sciences, Renmin University of China, Beijing, 100872, China*
[e] *Lab of Soft Matter and Biological Physics, Institute of Physics, Chinese Academy of Sciences, Beijing, 100190, China*
[f] *Institute of Wenzhou, University of Chinese Academy of Sciences, Wenzhou, 325001, China*

A B S T R A C T

Accurate drug delivery to the lesion has been deliberated for several decades, but one important phenomenon is usually neglected that the immune system can prevent smooth transportation of nanomedicine. Although injection would reduce first-pass effect, macrophages in the blood can still recognize and phagocytose nanomedicine. Here we show that a lubricated nanocontainer, which is prepared based on polyelectrolytes and mesoporous silica nanoparticles, can accurately target muscarinic bioreceptor while escaping from the identification of macrophages. Through *in vitro* and *in vivo* studies, this nanocontainer, combining both immune escape and bioreceptor targeting, has greatly improved the drug bioavailability. Additionally, this nanocontainer shows good biocompatibility, and the targeted heart tissues and other important metabolic organs, such as liver and kidney, keep physiological structures and functions without the detection of side effects. Furthermore, the mechanism of immune escape for the developed nanocontainer has been investigated by lubrication test and molecular simulation. We anticipate that our study will establish a new perspective on the achievement of immune escape-based targeted drug delivery, which can provide a fundamental approach for the design of related biomaterials.

1. Introduction

Immune escape and accurate targeting are considered as two effective methods to improve the proficiency of nanomedicine [1]. There has been considerable research on this area in the past few decades, but clearance by the mononuclear phagocyte system remains a barrier that may limit nanoparticle-mediated drug delivery [2–4]. In targeted drug therapy, the mesoporous silica nanoparticles (MSN) are widely employed for controlled drug delivery due to their good biocompatibility, structural rigidity, optical transparency, chemical stability, high surface area, and feasible surface modification [5]. Initially, the delivery of MSN to a region is achieved by controlling the size and surface charge

of the nanoparticles [6,7]. However, during the delivery process a certain amount of the encapsulated cargoes can still be released before arriving at the targeted site. Therefore, various chemical structures, such as nanovalves [8–12] and polymers [13–16], are designed and modified to the MSN surface, aiming to achieve an efficient targeted drug release. Additionally, some biomacromolecules with specific recognition function are also incorporated onto the MSN surface, further improving the targeting effect [17].

Indeed, accurate localization to the lesion can remarkably increase the bioavailability and also reduce the occurrence of side effects. However, nanoparticles still need to break through various defenses when being delivered in the human body. Particularly, the immune
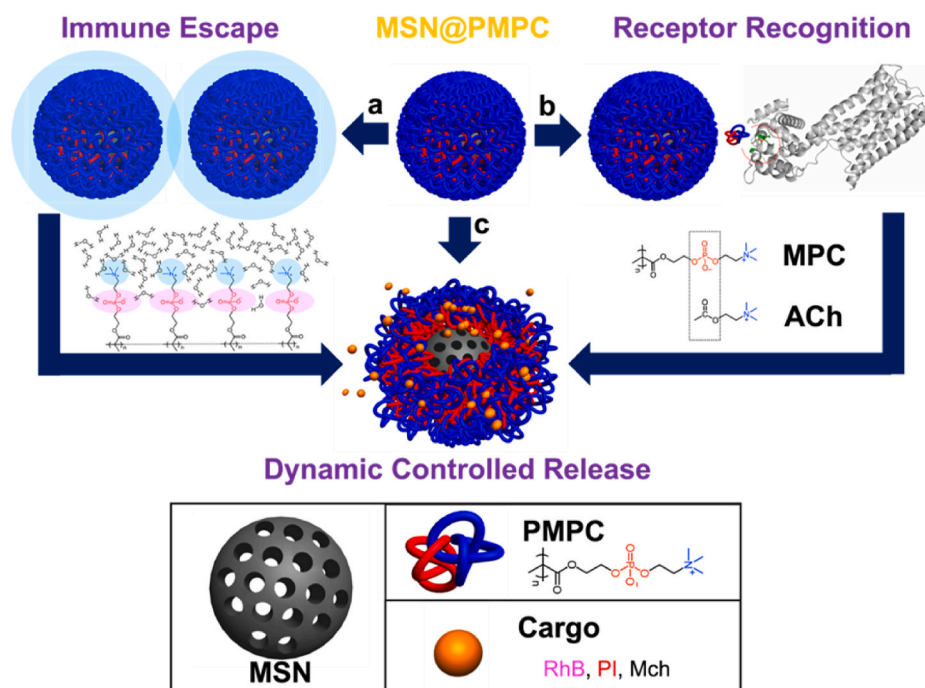

Fig. 1. The schematic diagram of the nanocontainer (MSN@PMPC) with multi-functional properties. The PMPC polymers are modified on the surface of MSN based on LbL due to the ion-dipole interactions. **a** hydration-induced immune escape, **b** bioreceptor recognition, and **c** controlled release of pre-loaded cargoes.

system can protect the host from foreign substances by interacting with the chemical or biological entities, resulting in the immunostimulation and immunosuppression [18]. Macrophages, as an essential component of the third barrier of the immune system, can recognize nanoparticles to be foreign substances and therefore phagocytosis dramatically reduces the treatment effect [19]. However, macrophages have defects in the process of recognition and phagocytosis of the nanoparticles. It is accepted that the interaction between the macrophages and the nanoparticles is determined by nanoparticle size, surface charge, hydrophobicity/hydrophilicity, etc. Additionally, the steric effect of polymer coatings on the surface of nanoparticles can mediate the interaction with the macrophages. For example, nanoparticles can be grafted with poly (ethylene glycol) (PEG) or other kinds of polymers to provide a hydrophilic environment, thus shielding them from the recognition by the macrophages [20].

Therefore, a few bio-friendly hydrophilic polymers, for example PEG, are considered to be able to reduce phagocytosis of macrophages as the recognition mechanism is based on surface hydrophilicity [21]. Additionally, PEG can be modified with controllable chemical structure at its two terminals and effectively improve the targeting effect of nanoparticles. Recently, poly(2-(methacryloyloxy)ethyl phosphorylcholine) (PMPC) has been widely employed for hydration lubrication because the zwitterionic charges can induce a dense water layer on the surface [22], therefore it may generate an enhanced hydrophilic capability to escape from the identification of macrophages. More importantly, the PMPC monomer (MPC) has a potential on binding with muscarinic acetylcholine receptors (M receptors) due to the similar structure with acetylcholine (ACh). It is accepted that ACh is the primary neurotransmitter released by the heart under the innervation of parasympathetic nerve. Consequently, the binding of ACh with M receptors is very important in the treatment of the disease of tachycardia as the heart rate is regulated by the parasympathetic nerves. From this viewpoint, PMPC, which can provide a super-hydrophilic surface and the recognition function, has become a suitable option to achieve higher efficiency of in the treatment of disease that is related to M receptors.

In the present study, we propose a lubricated nanocontainer (MSN@PMPC) prepared by layer-by-layer (LbL) approach, which can achieve macrophages escape (Fig. 1a), bioreceptor targeting (Fig. 1b), and controlled drug release (Fig. 1c) via the modification of PMPC on the surface of MSN. Compared with the traditional drug release systems, our design processes a function of immune escape due to the superhydrophilic lubricated surface, which shields the MSN@PMPC from the identification by the surrounding macrophages. Besides, according to the competitive binding mechanism, the phosphorylcholine structure in MSN@PMPC, which is similar to that of ACh, is responsible for achieving bioreceptor recognition and targeted drug release. After arriving at the targeted site, the PMPC on the surface of the nanocontainer, which has priority over M receptors with a higher binding constant, will dissociate from MSN@PMPC and thus release the pre-encapsulated cargoes. Technically, the preparation of MSN@PMPC is simple with a reasonable cost, which is expected to achieve industrial production. In this study, rhodamine B (RhB), propidium iodide (PI), and methacholine (MCh, agonist for M receptors) are loaded separately into MSN@PMPC in order to examine the properties of controlled release, immune escape, and bioreceptor recognition, respectively. Overall, the design of the lubricated nanocontainer demonstrates excellent receptor recognition ability while avoiding phagocytosis of the macrophages.

2. Materials and methods

2.1. Synthesis of lubricated nanoparticles

The functional MSN (including MSN-COOH and MSN-NH$_2$) was synthesized according to the procedures reported in our previous works [14,23], which was also provided in Supporting Information. The lubricated nanoparticles (i.e. cargo-loaded MSN@PMPC) were prepared by soaking MSN (20 mg) in an aqueous solution of the cargoes (0.5 mmol L^{-1} in phosphate buffer solution (PBS), 10 mL, pH = 7.4) for 5 h at room temperature. Afterwards, PMPC (15 mg) was dissolved in PBS (1 mL, pH = 7.4) and added to the above solution. The mixture was sonicated and stirred for 15 min. Subsequently, the solution was centrifuged at 8000 rpm for 1 min, and the precipitate was redispersed into another batch of fresh PBS with PMPC. The procedure was repeated three times

to prepare the cargo-loaded MSN@PMPC. Finally, the nanoparticles were washed with PBS (pH = 7.4) three times and lyophilized for storage. During the cargo-loading process, the cargoes could diffuse into the mesopores of the nanoparticles gradually until the concentration difference inside and outside of the nanoparticles was balanced. Additionally, the supramolecular interactions between the nanoparticles and the cargoes also contributed to cargo absorption on the surface of the nanoparticles. (cargo: RhB, PI, and MCh; carboxylic modified MSN: MSN-COOH; aminated MSN: MSN-NH$_2$). The loading efficiency of different cargoes into the nanoparticles was evaluated using an ultraviolet spectrophotometer (UV-8000s, Metash Instruments, Shanghai, China), and the result was shown in Table S1 in Supporting Information.

2.2. Material characterizations

Small-angle X-ray diffraction (XRD) profile was obtained on a d/max 2550 V diffractometer (Rigaku, Japan) over a 2θ range from 0.6° to 10° at a scanning speed of 2° min^{-1}. The radiation source of the diffractometer was copper (Kα = 1.54184 Å). Nitrogen adsorption/desorption isotherm was measured employing a Tristar 3020 M instrument (Micromeritics, USA). Specific surface area was calculated using the adsorption data in the low-pressure range based on the Brunauer−Emmett−Teller (BET) model, and pore size distribution was determined according to the Barrett−Joyner−Halenda (BJH) method. Scanning electron microscope (SEM) image was examined by a Quanta 200 FEG instrument (FEI, Netherlands). Au–Pd coating used for imaging was performed by sputtering for 120 s with a Gatan 682 precision etching & coating system (Gatan, USA). Transmission electron microscopy (TEM) image was collected using a HT7700 instrument (Hitachi, Japan), with an accelerating voltage of 100 kV. Fourier transform infrared (FTIR) spectrum was recorded employing a Vertex 70 spectrometer (Bruker, Germany) with a wavelength from 600 cm^{-1} to 4000 cm^{-1}. Thermogravimetric analysis (TGA) was performed using a Q5000 instrument (TA Instrument, USA) at a heating rate of 10 °C min^{-1} from 25 °C to 900 °C. Controlled release profile at different temperatures was obtained via by a Cary 7000 UV–vis spectrophotometer (Agilent Technologies, USA). Lubrication test was performed using an atomic force microscope (AFM, MFP-3D, Asylum Research, Santa Barbara, USA) under contact mode.

2.3. Controlled drug release

The cargo-release mechanism is mainly based on the concentration difference between the inside and outside of the nanoparticles. Generally, the drug release experiment was performed using a homothermal shaker at different temperatures. RhB was set as the model molecule. The RhB-loaded MSN-COOH and RhB-loaded MSN-COOH@PMPC nanoparticles (5 mg) were uniformly dispersed in PBS (1 mL, pH = 7.4), transferred to a dialysis bag, and dialyzed against their corresponding buffer solution (20 mL) in capped beaker under stirring at 37 °C or 50 °C. At every designated interval, the buffer solution (4 mL) in the beaker was taken out, and fresh buffer solution (4 mL) was replenished to keep a constant volume. The amount of RhB released into the buffer solution was calculated using the spectrophotometer at a wavelength of 565 nm. The concentration of RhB released from the nanoparticles was expressed as a percentage of the total RhB loaded in the nanoparticles and plotted as a function of time. The cumulative RhB release was calculated by the equation as shown below, where M_t and M_∞ are the amount of RhB released from the nanoparticles at time t and time infinity.

$$\text{Cumulative RhB release (\%)} = M_t/M_\infty \times 100\%$$

2.4. Lubrication test

The dynamic friction between PMPC-coated SiO$_2$ wafer and PMPC-coated colloidal probe under various aqueous suspensions of the nanoparticles was measured using the AFM under contact mode. Firstly, the amination of the SiO$_2$ wafer was performed by adding a few drops of aminopropyltriethoxysilane (APTES) solution (72% v/v ethanol, 8% v/v water, and 20% v/v APTES) on the surface. After 12 h, the wafer was sonicated to remove free APTES molecules. Subsequently, the wafer was immersed in the aqueous solution of MPC (0.05 mol L^{-1}) with a few drops of tert-butyl hydroperoxide (TBHP). The grafting of PMPC was proceeded under nitrogen atmosphere at 80 °C for 12 h, and finally the wafer was washed by deionized water sufficiently in order to remove the unreacted molecules. Secondly, the aminated polystyrene microsphere (diameter: 5 μm) aqueous suspension (0.5 mL) was added to the aqueous solution of MPC (0.05 mol L^{-1}) with a few drops of TBHP as the initiator. Similarly, the grafting of PMPC was achieved under nitrogen atmosphere at 80 °C for 12 h, after which the PMPC-coated polystyrene microspheres were collected by centrifugation and dried under vacuum. Afterwards, the microspheres were glued onto the jut of AFM cantilever under UV-irradiation for 40 min according to our previous work [24].

Four different lubrication media were prepared with deionized water, 0.025 mg mL^{-1}, 0.05 mg mL^{-1}, and 0.1 mg mL^{-1} of MSN-COOH@PMPC aqueous suspensions, respectively. These samples were sonicated for 5 min to uniformly disperse the nanoparticles. The spring constant of the probe (type: TL-CONT) was determined by the frequency method [25], and the lateral sensitivity of the probe was characterized by the improved wedge calibration method [26]. The lubrication test was performed at room temperature under various loads in the range from 50 nN to 200 nN, a sliding distance of 20 μm, and a frequency of 1 Hz. The load was added once every 64 sliding cycles to get a 256-cycle-friction map. Under each situation, three rectangle locations (20 μm × 20 μm) were randomly chosen to run the lubrication test under the same gradient of load, i.e. 50 nN, 100 nN, 150 nN, and 200 nN, respectively. The friction coefficient (COF) was calculated as the value of the lateral force divided by the normal load.

2.5. Macrophage phagocytosis

Macrophages (RAW 264.7) were cultured in RPMI-1640 medium with 10% fetal bovine serum, penicillin (100 mg mL^{-1}), and streptomycin (100 mg mL^{-1}) at 37 °C and 5% CO$_2$. One day before the experiment, macrophages were seeded on cell culture dish (diameter: 29 mm, glass bottom) coated by collagen at a density of 1×10^6 cells mL^{-1}. Subsequently, the cells were incubated with PI-loaded MSN-COOH and PI-loaded MSN-COOH@PMPC (0.1 mg mL^{-1}) for 3 h at 37 °C and 5% CO$_2$. After that the cells were fixed with 4% paraformaldehyde and washed three times with PBS (0.10 mol L^{-1}, pH = 7.4). The nucleus was stained by Hoechst 33342 (1 g mL^{-1}) for 30 min, and the membrane was stained by DIO cell-labelling solution for 30 min (5 μL of supplied dye labelling solution was added into 1 mL of normal growth medium). Then the cells were washed three times with PBS after dyeing each time. Finally, the fluorescent images were acquired by a Leica SP-8 confocal laser scanning microscope (Leica Microsystems, Wetzlar, Germany) with a 25 × magnification/0.95 N$_A$ water immersion objective and quantified using an ImageJ software (National Institutes of Health, Bethesda, MD, USA) for quantitative evaluation of the fluorescence intensity.

2.6. Molecular simulation

Molecular simulation was performed following three procedures including molecular model building, computational complex prediction, and receptor-ligand interaction energy calculation. Firstly, the sequence of M2 (homo sapiens, one typical M receptor) was obtained from National Center for Biotechnology Information database, and its 3D structure was constructed utilizing the comparative protein structure

modelling tool Modeller [27] and the unified protein structure prediction platform I-TASSER [28]. The best models from the Modeller and I-TASSER were chosen and further minimized using molecular dynamics simulation package Gromacs 4.5 [29] based on optimized potentials for liquid simulations (OPLS) force field [30]. The model with the optimal energy score was selected and then used for the following computational analysis. In addition, the 3D structures of MPC and ACh were constructed using Gaussian software and obtained from protein data bank. Secondly, the complex formed by receptor-ligand interaction between M2 and MPC (M2-MPC) and between M2 and ACh (M2-ACh) was predicted using the molecular docking approach HoDock [31], from which a refined semi-flexible docking was achieved based on Monte Carlo method following an initial rigid setup. The prediction of the binding sites was implemented to reduce docking sampling space and eliminate unreasonable docked structures. The complex was visualized by PyMOL software (http://www.pymol.org/), and a minimization process was performed using Gromacs 4.5 to obtain reasonable interaction energy. Finally, the total interaction energy of M2-MPC and M2-ACh complex was analyzed using a web-based software PEARLS (Program for Energetic Analysis of Ligand-Receptor Systems, http://ang.cz3.nus.edu.sg/cgi-bin/prog/rune.pl) [32], with the calculation of Van der Waals energy, electrostatic energy, and hydrogen bond energy between the binding molecules. The values of solvation free energy of molecular binding and ligand conformational entropy were also obtained by this program.

2.7. In vitro cytotoxicity

Human liver cell line (QSG-7701), human embryonic kidney cell line (HEK-293), and HeLa cell line were cultured in the Dulbecco's Modified Eagle Medium containing 10% fetal bovine serum, penicillin (100 mg mL^{-1}), and streptomycin (100 mg mL^{-1}) at 37 °C and 5% CO_2. Subsequently, the cells were seeded on a 96-well culture plate at a density of 5000 cells per well and then co-cultured with MSN-COOH, PMPC, and MSN-COOH@PMPC, respectively for 24 h. Afterwards, 10 μL of Cell Counting Kit-8 (CCK-8, Dojindo Kagaku, Japan) working solution was added into each well and co-cultured with the cells for another 3 h. The absorbance of the solution was measured by a microplate reader (Infinite F50, Tecan, Switzerland) at a wavelength of 450 nm.

2.8. In vivo mice study

Sixty 12-week-old male mice (C57BL/6) with natural tachycardia model were purchased from Beijing Vital River Laboratory Animal Technology Co., Ltd and bred in the Experimental Medical Research Center of Ruijin Hospital. The mice were fed with standard chow and tap water ad libitum in a lab maintaining at 22 ± 2 °C (12 h light-dark cycle). All the procedures were strictly performed in accordance with the Guidelines for the Care and Use of Laboratory Animals. It was noted that the experimental details of the *in vivo* rat study were provided in Supporting Information.

2.9. Administration treatment

The mice were randomly divided into the following four groups (n = 15 for each group) including (1) saline group, (2) MSN-COOH@PMPC (3.6 mg kg^{-1}) group, (3) MCh-loaded MSN-COOH (4.0 mg kg^{-1}) group, and (4) MCh-loaded MSN-COOH@PMPC (4.0 mg kg^{-1}) group. Generally, the MCh-loaded MSN-COOH group and MCh-loaded MSN-COOH@PMPC group contained about 0.4 mg kg^{-1} of MCh. MCh was uniformly dissolved in 0.9% saline, and MSN-COOH@PMPC, MCh-loaded MSN-COOH, and MCh-loaded MSN-COOH@PMPC were suspended in 0.9% saline by ultrasonic dispersion for 2 min. The materials were injected into the mice through tail vein in groups (2), (3), and (4) for 10 consecutive days, respectively. The mice in group (1) were administered an equal volume of 0.9% saline in the same schedule. Specifically, the mice were placed in a holder with the tail exposed to facilitate the injection of materials into tail vein (the blood compatibility of the functional nanoparticles was tested, and the results were shown in Fig. S1). The tail of the mice was straightened and sterilized with 75% alcohol. The junction of the mid-distal section of the tail was selected to be the puncture site, and 200 μL of the materials was gently injected using a sterile syringe. After the puncture site stopped bleeding, the mice were grasped and fixed on the cardboard in order to perform the electrocardiogram (ECG) recording. Since the mice were administered for 10 consecutive days, the puncture site was changed from far to near of the junction in the mid-distal section of the tail and then the other side.

2.10. ECG recording and analysis

At about the same time every day, the mice were brought to the experiment room in advance to allow the mice to fully adapt to the environment and not to affect the measurement of heart rate. The reference electrode, positive electrode, and negative electrode of standard limb lead system were inserted under the skin of right hindlimb, left hindlimb, and right forelimb of the mice via a needle electrode, respectively (Fig. S2). When the breathing of the mice was stable, ECG recording was started and continued for a duration of 5 min employing a BioAmp and PowerLab system (FE136 and PowerLab 8/35, ADInstruments, Australia). Afterwards, the electrodes were removed, and the mice were returned to the breeding room. The recorded ECG of each mouse was checked, and the section with a stable recording (longer than 10 s) was selected to determine the desired parameters including heart rate, PR interval, QRS interval, QT interval, P wave duration, P amplitude, R amplitude, T amplitude, and Tpeak tend interval. The measurement method of the parameters was shown in Figs. S3–S11. The parameters were obtained and further imported to the Statistical Product and Service Solutions software (SPSS Inc., Chicago, IL, USA) for statistical analysis.

2.11. Histological analysis and immunohistochemistry

The mice were sacrificed with inhaling anesthesia using isoflurane until breathing stopped. The abdominal cavity of the mice was cut with scissors, and the diaphragm and chest wall were cut from the end of the incision to the head of the mice. The sternum was turned up to fully expose the heart. Subsequently, the right atrial appendage was cut to allow the blood to flow out of the body. An injection of saline into the left ventricle was performed to flush the blood out of the mice until the liver and lungs appeared normal. The heart was fixed by injecting 4% paraformaldehyde (10 mL) into the left ventricle and cut with scissors to remove the connective tissues. The heart was put in 4% paraformaldehyde to fix for 48 h, embedded in paraffin, and dissected into serial sections with a thickness of 5 μm. Afterwards, the sections were analyzed by hematoxylin and eosin staining to examine the morphology of the heart tissue and to measure the left ventricular long and short axis length and the ventricular septal thickness. Additionally, the immunohistochemical staining was performed employing the anti-ADCY5 or anti-CHRM2 antibodies produced in rabbit (1:100) for 24 h at 4 °C and horseradish peroxidase-linked anti-rabbit antibody (1:500) for 60 min at room temperature. Then the slides were incubated by 3,3′-diaminobenzidine and counterstained with hematoxylin. The images of the slides were captured using an optical microscope (BX61TRF, Olympus, Tokyo, Japan) and quantified by the ImageJ software to quantitatively characterize the content of the target proteins in the tissues.

2.12. Immunofluorescence staining and hematoxylin and eosin staining

The heart, liver, and kidney tissues were collected and fixed in 4% paraformaldehyde. Then these tissues were embedded in paraffin and dissected into transverse sections with a thickness of 5 μm. Regarding with the heart tissues, immunofluorescence staining was performed with the anti-α-actinin antibody (1:150). A digital scanner (Pannoramic

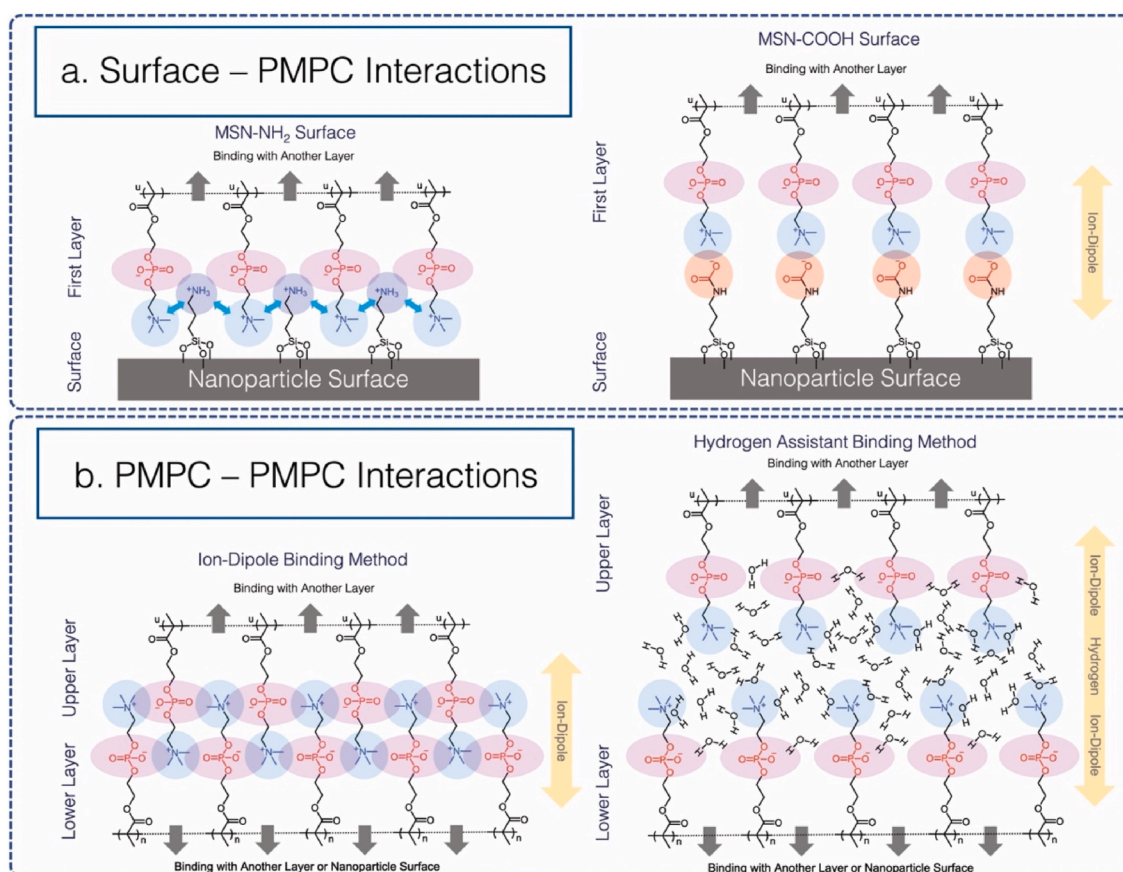**Fig. 2.** The synthetic mechanism of the lubricated nanoparticles. **a** The binding behavior of PMPC with MSN surface. The binding mode of PMPC with MSN-NH$_2$ (left): the amino groups from MSN form an ion-dipole interaction with the -PO$_4^-$; however, the repulsive force from the –N(Me)$_3^+$ pushes PMPC away from the surface. The binding mode of PMPC with MSN-COOH (right): the mechanism of the coating is due to a dipole-dipole interaction between the –N(Me)$_3^+$ of PMPC and the –COO$^-$ from MSN surface. **b** The binding behavior of PMPC on MSN surface with multiple pots of coating: the ion-dipole binding method (left) and hydrogen bond assistant binding method (right).

MIDI, Villepinte, France) was used to capture the images. For the liver and kidney tissues, the sections were analyzed by hematoxylin and eosin staining to observe the structures. An optical microscope (H550S, Nikon Corporation, Japan) was used to capture the images.

2.13. Primary cardiomyocyte apoptosis

The heart tissues from 3-day-old neonatal mice were cut into small pieces and then digested with an enzyme mixture (containing 0.08% trypsin and 0.05% collagenase type II) for 5 min at room temperature for three times. Subsequently, the tissue lysates were collected and blended with an equal volume of the culture medium containing DMEM/F-12, 15% fetal bovine serum, 1% penicillin-streptomycin, and 0.1 mmol L^{-1} of bromodeoxyuridine. After centrifugation at 1000 rpm for 10 min, the cells were resuspended in 10 mL of the culture medium and incubated for 60 min. The supernatant was collected into the 65-mm Petri dish, and the cardiomyocytes adhered to the Petri dish after culturing for 48 h. Afterwards, the cardiomyocytes were received different stimulations by MSN-COOH and MCh-loaded MSN-COOH@PMPC and continued to culture for 48 h. The control group was only replaced with fresh medium, and the media of the MSN-COOH and MCh-loaded MSN-COOH@PMPC groups contained 0.1 mg mL^{-1} of the corresponding nanoparticles.

2.14. Flow cytometry

The cardiomyocytes were harvested and centrifuged at 500 g for 5 min at 4 °C, and then the supernatant was aspirated. The

cardiomyocytes were washed with 1 mL of PBS. Afterwards, 2 μL of Annexin V and 2 μL of PI were mixed in 100 μL of the staining buffer and resuspended according to the manufacturer's instructions. Then the cardiomyocytes were incubated for 15 min at room temperature in the dark. After centrifugation at 500g for 5 min at 4 °C, the staining buffer was aspirated, and the cardiomyocytes were resuspended in 100 μL of PBS. Finally, the samples were analyzed by fluorescence activated cell sorting (FACS) using a flow cytometer (CytoFLEX, Beckman Coulter, USA). A laser with a wavelength of 488 nm was employed for excitation. Based on the value of fluorescence intensity of Annexin V and PI, the cells could be classified into double negative cardiomyocytes (healthy), PI positive cardiomyocytes (necrosis), Annexin V positive cardiomyocytes (early apoptosis), and double positive cardiomyocytes (late apoptosis), respectively.

2.15. Western blot

The protein lysates were initially obtained from the cultured primary cardiomyocytes. An equal amount of protein (30 μg) was separated by sodium dodecyl sulfate polyacrylamide gel electrophoresis and electrotransferred to a polyvinylidene fluoride membrane. The membrane was incubated with anti-caspase 3 and anti-cleavage caspase 3 (1:1000) or Glyceraldehyde 3-Phosphate Dehydrogenase (GAPDH, 1:5000) primary antibodies at 4 °C overnight, and then incubated in horseradish peroxidase coupled with rabbit or mouse IgG (1:2000) for 1 h at room temperature. Finally, the membrane was washed for three times, and the immunoreactive bands were visualized by an Odyssey Infrared Imaging System (LI-COR, Inc., Lincoln, MT, USA). The density of each band was
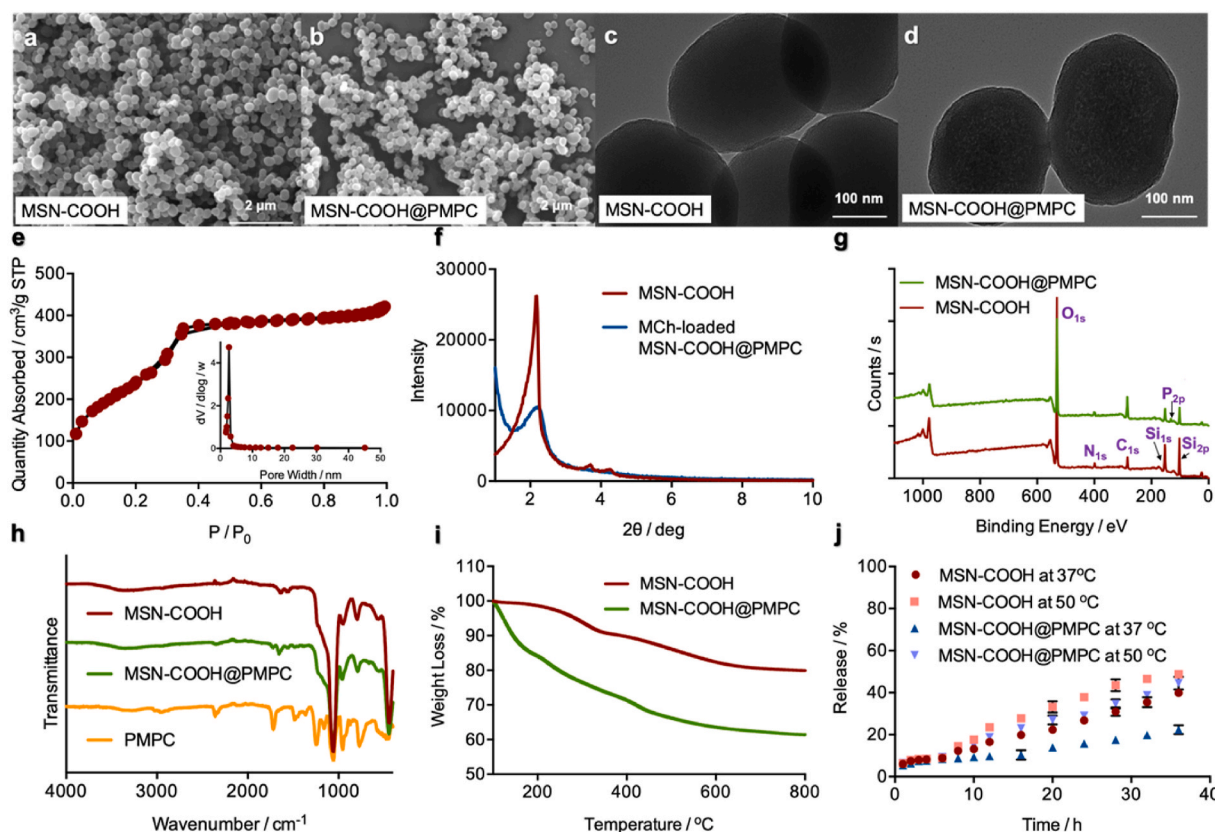
Fig. 3. The morphological and structural characterizations of the lubricated nanoparticles. Morphological characterization: SEM images of **a** MSN-COOH and **b** MSN-COOH@PMPC; TEM images of **c** MSN-COOH and **d** MSN-COOH@PMPC. Structural characterization: **e** BET and BJH (insert) of MSN-COOH; **f** XRD patterns of MSN-COOH (red) and MCh-loaded MSN-COOH@PMPC (blue). Surface coating and release behavior characterizations: **g** XPS spectra of MSN-COOH (red) and MSN-COOH@PMPC (green); **h** FTIR spectra of MSN-COOH (red), MSN-COOH@PMPC (green), and PMPC (orange); **i** TGA curves of MSN-COOH (red) and MSN-COOH@PMPC (green); **j** Drug release profiles of RhB-loaded MSN-COOH and RhB-loaded MSN-COOH@PMPC at two different temperatures: MSN-COOH at 37 °C (red), MSN-COOH@PMPC at 37 °C (blue), MSN-COOH at 50 °C (pink), and MSN-COOH@PMPC at 50 °C (purple).

quantified using the ImageJ software.

3. Results and discussion

3.1. Synthetic mechanism of MSN@PMPC

We have examined the LbL self-assembly technique on the MSN surface in a previous study, as a practical approach, to develop a high-efficient hybrid nanocontainer for the release of anti-cancer drug [14]. In this design, the charged PMPC polymers are coated on the MSN surface due to the ion-dipole interactions between the interfaces. To investigate the coating mechanism of PMPC on the MSN surface, both MSN-NH$_2$ and MSN-COOH have been chosen to examine the effect on different surface charges (Fig. 2). In Fig. 2a, MSN-NH$_2$ switches the surface to positive charge, and the $-NH_3^+$ groups on the surface can form interactions with the phosphate groups. However, the strong repulsive force also pushes the PMPC molecules away from the surface. On the contrary, the negative dipoles in MSN-COOH form dipole-dipole interactions with the $-N(Me)_3^+$ groups of PMPC due to charge transfer. The farther phosphate groups from PMPC do not cause any significant repulsion for the binding. To prove the prediction of binding modes, MSN-NH$_2$ and MSN-COOH are prepared for the loading of cargo (RhB) and coating of PMPC. The encapsulation efficiency of the nanoparticles has been calculated based on UV–*vis* absorption (Fig. S12 and Fig. S13). The result demonstrates that MSN-COOH@PMPC presents a much higher encapsulation efficiency than MSN-NH$_2$@PMPC owing to the stronger binding mode. Therefore, the following experiments use MSN-COOH@PMPC to characterize the properties of the nanoparticles.

To achieve effective control by increasing the coverage of PMPC on the surface, the amount of PMPC is typically divided into several parts to cover the surface of MSN (Fig. 2b). The first part of PMPC, as the lowest layer, binds both the surface of MSN and the upper layer of PMPC. The upper layer inserts into the lower layer, forming an interaction pair among the $-N(Me)_3^+$ and phosphate groups. According to hydration lubrication mechanism [22], the highly charged PMPC can easily form a water layer on the surface before the resulting coating layer. The water layer can bind with the following layer due to hydrogen bonds, which assist the further assembly and coating on the surface of MSN. The advantage of multiple coating of PMPC is confirmed by thermogravimetric analysis (TGA), which shows ca. 20% more PMPC has been assembled on the surface of MSN-COOH by taking multiple pots of coating (Fig. S14).

3.2. Material characterizations

The functional nanoparticles are evaluated based on scanning electron microscope (SEM), transmission electron microscope (TEM), nitrogen adsorption/desorption isotherm (BET & BJH), and small-angle X-ray diffraction (XRD). The SEM and TEM (Fig. 3a–d) images demonstrate that the nanoparticles are spherical, with an average size of ca. 240 nm in diameter (Fig. S15). Before PMPC coating on the surface, MSN-COOH exhibits uniformly sized and 2D-hexagonally ordered cylindrical pores (MCM-41 type). After PMPC coating on the surface, MSN-COOH@PMPC still remains the same shape, but it hardly shows the porous structure. In Fig. 3e, an adsorption step at the relative pressure (P/P$_0$) value of 0.1–0.3 for MSN-COOH exhibits characteristic type IV
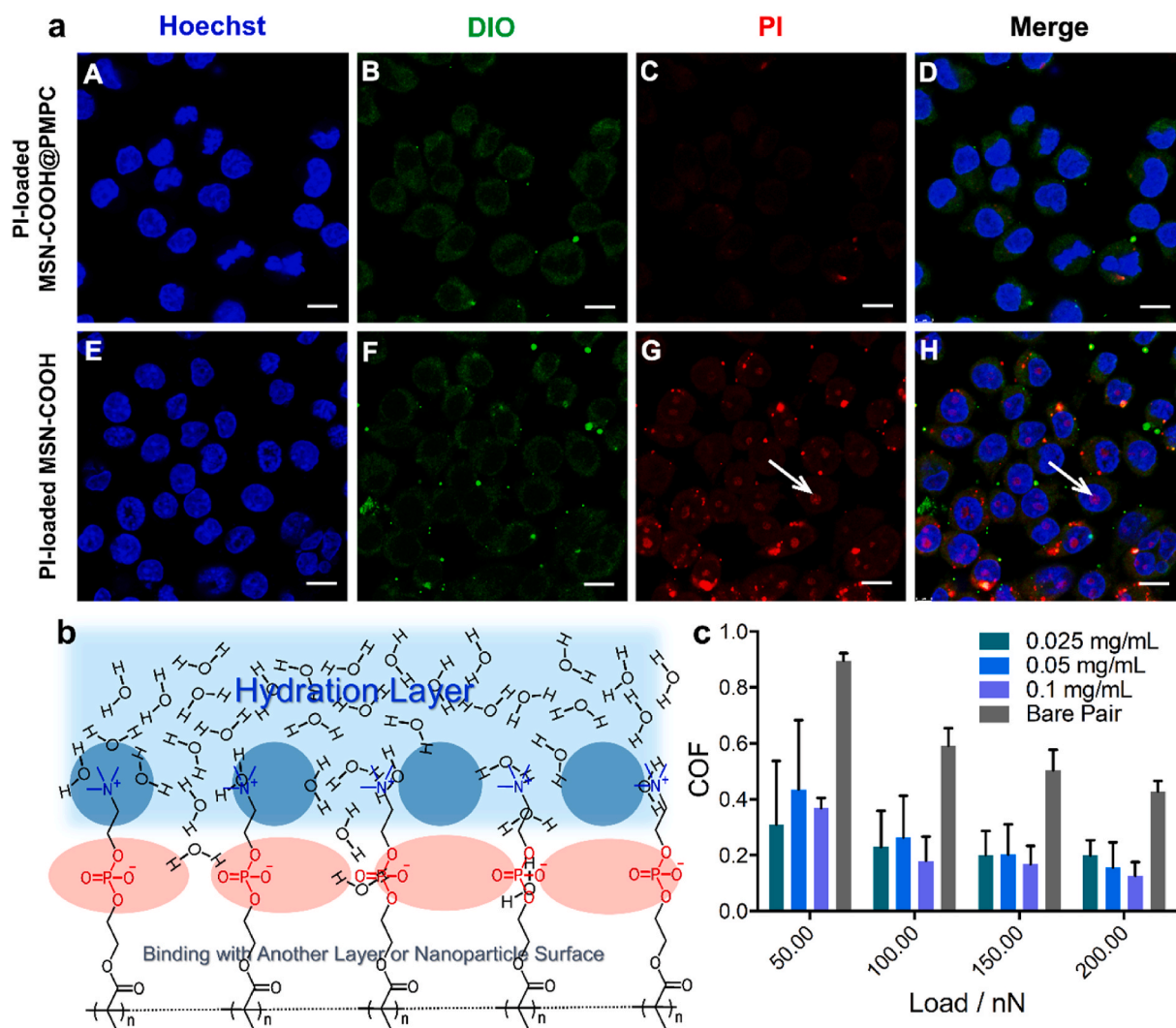
Fig. 4. Cell uptake experiment for the mechanism of macrophage escape: **a** The engulfment of PI-loaded MSN-COOH@PMPC (**A-D**) and PI-loaded MSN-COOH (**E-H**) by macrophages. Macrophages are incubated with PI-loaded MSN-COOH and PI-loaded MSN-COOH@PMPC (0.1 mg mL^{-1}) for 3 h, after that fixed and stained. The following cellular organelles are stained selectively based on standard protocols: cell membranes & lipids (DIO cell-labelling solution, 5 μL of the supplied dye labelling solution is added into 1 mL of normal growth medium) and nuclei (Hoechst, 1 μg mL^{-1}). (**A, E**) Nuclei (blue channel, $\lambda_{ex} = 405$ nm, $\lambda_{em} = 450 \pm 30$ nm. (**B, F**) Cell membranes (green channel, $\lambda_{ex} = 488$ nm, $\lambda_{em} = 515 \pm 15$ nm). (**C**) PI-loaded MSN-COOH@PMPC (red channel, $\lambda_{ex} = 552$ nm, $\lambda_{em} = 617 \pm 15$ nm). (**G**) PI-loaded MSN-COOH (red channel, $\lambda_{ex} = 552$ nm, $\lambda_{em} = 617 \pm 15$ nm). (**D**) An overlay of (**A**)−(**C**). (**H**) An overlay of (**E**)−(**G**). The multi-colour confocal microscopic images indicate that PI-loaded MSN-COOH has been localized into the cells after 3 h. The appearance of nuclear costaining (violet) indicates the release of PI from PI-loaded MSN-COOH to the nucleus of the cells (**G**). Scale bars: 10 μm **b** The prediction for mechanism of macrophage escape based on the formation of a hydration layer surrounding the zwitterionic headgroups in PMPC. **c** The measurement of COF for bare tribopair (grey) and MSN-COOH@PMPC tribopairs with different concentrations (n = 3; 0.025 mg mL^{-1}, green; 0.05 mg mL^{-1}, blue; 0.1 mg mL^{-1}, purple).

isotherm, confirming the presence of mesoscale pores [33]. The step is obtained due to nitrogen condensation inside the mesopores via capillarity. Additionally, an obvious step is displayed at the relative pressure ranging from 0.2 to 0.7, which is attributed to capillary condensation of nitrogen inside the primary mesoporous nanoparticles. A narrow Barrett−Joyner−Halenda (BJH) pore size distribution is indicated in accordance with the steep condensation step (the inset of Fig. 3e). After cargo loading and PMPC coating, the specific surface area (S$_{BET}$) of RhB-loaded MSN-COOH@PMPC remarkably reduces to 547.27 m^2 g^{-1} in comparison with that of MSN-COOH (878.59 m^2 g^{-1}), as shown in Fig. S16 and Table S2. Fig. 3f shows the XRD patterns of MSN-COOH and MCh-loaded MSN-COOH@PMPC. The main crystal face {100} of MCh-loaded MSN-COOH@PMPC moves to the larger degree compared with that of MSN-COOH, indicating that the cargo and PMPC have been successfully loaded and coated with MSN-COOH, respectively. The calculation of microstructures based on nitrogen adsorption/desorption isotherm and XRD is shown in Table S2. All the calculation details are

provided in Supporting Information.

The surface compositions of MSN-COOH and MSN-COOH@PMPC are collected by XPS (Fig. 3g and Fig. S17) and FTIR (Fig. 3h) spectra. Compared with MSN-COOH, the phosphorus (P 2p) from PMPC is identified in XPS for MSN-COOH@PMPC. In addition, no new peaks are observed in FTIR as the LbL approach does not induce any chemical reactions. The TGA curves of MSN-COOH and MSN-COOH@PMPC are shown in Fig. 3i and Table S3. The weight losses are detected from 180 °C to 800 °C. Below 180 °C, MSN-COOH@PMPC generates a sharp weight loss (ca. 14.5%), which is attributed to the physical loss of the bounded water. This confirms the formation of a hydration layer (ca. 5 nm thickness, the calculation is provided in Supporting Information) surrounding the zwitterionic headgroups in PMPC. The proportion of the PMPC polymers that are coated on the surface of MSN by LbL self-assembly is approximately 22%. The reason we choose LbL approach rather than one single layer coating is investigated by TGA, as shown in Fig. S14. The TGA curve of LbL coating loses ca. 10% more weight than
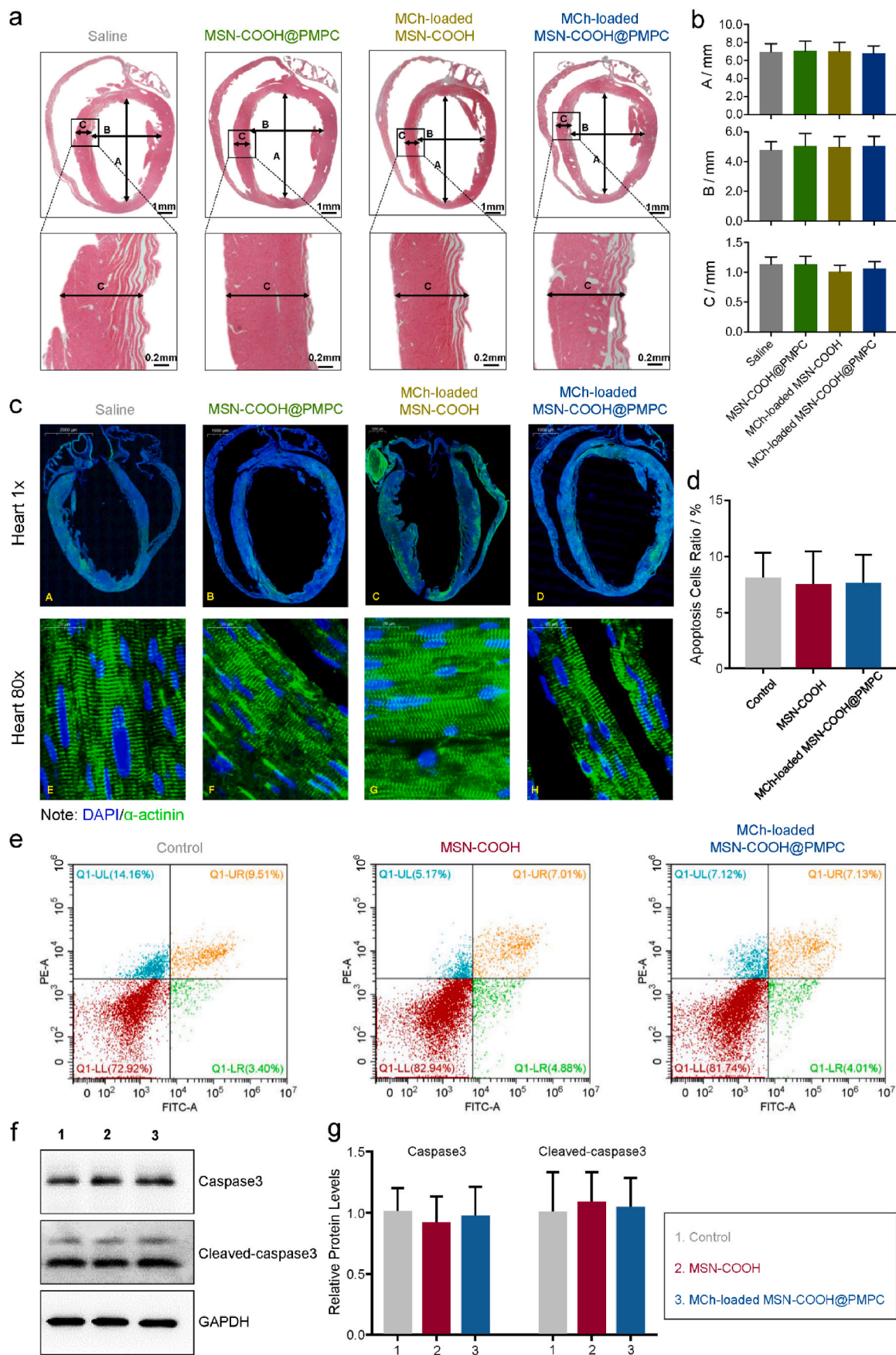
Fig. 5. The *in vivo* biocompatibility of the nanoparticles. **a** Tissue slides of mice heart after treating with saline, MSN-COOH@PMPC, MCh-loaded MSN-COOH, and MCh-loaded MSN-COOH@PMPC. **b** Statistical analysis of the size of the heart tissues at the position of A (left ventricular long axis length), B (left ventricular short axis length), and C (ventricular septal thickness) as displayed in **a**, n = 5. **c** The effect of MCh-loaded MSN-COOH@PMPC on the arrangement of myocardial sarcomere, compared with saline, MSN-COOH@PMPC, and MCh-loaded MSN-COOH. **d** The effect of MCh-loaded MSN-COOH@PMPC on cardiomyocyte apoptosis compared with saline and MSN-COOH, n = 5. **e** Flow cytometry for the proportion of apoptotic cardiomyocytes with saline, MSN-COOH, and MCh-loaded MSN-COOH@PMPC. The upper right quadrant of the chart indicates the proportion of apoptotic cardiomyocytes. FITC-A stands for Annexin V, and PE-A stands for PI. **f** Protein expression of caspase3 and cleaved caspase3 in primary cardiomyocytes detected by western blot. **g** Quantitative analysis of the relative expression of apoptosis-related proteins for caspase3 and cleaved caspase3, n = 5.

---

that of one single layer coating, which indicates that the LbL approach forms a much denser and more stable layer on the surface of MSN. Fig. 3j shows the drug release profiles of RhB-loaded MSN-COOH and RhB-loaded MSN-COOH@PMPC at the temperature of 37 °C and 50 °C, indicating that the nanoparticles provide a controlled drug release behavior. During the cargo-loading process, the supramolecular interactions between the nanoparticles and the cargoes contribute to cargo absorption onto the surface of the nanoparticles in addition to the concentration difference effect. The binding strength of the supramolecular interactions depends on temperature, and it is accepted that a higher temperature can weaken the absorption and enhance dissociation of the cargoes from the surface of the nanoparticles. Therefore, the cargo release profile shows an increasing amount of the cargoes when the temperature rises. Additionally, the relatively slow cargo release from the nanoparticles is attributed to the multi-layers of dense zwitterionic polymers on the surface, which was similar to the results of our previous study [14]. The mechanism of coating PMPC polymer on the surface of MSN is based on supramolecular ion-dipole interaction. The purpose of choosing a higher temperature can prove that PMPC has been coated on the surface of MSN rather than physical mixing.

3.3. Immune escape behavior and mechanism

Macrophages are typical phagocytic cells in the human body, which play an important role in identifying and internalizing foreign substances from external environment [34]. Although the nanoparticles are often first identified by the macrophages, they can be specifically modified to either target or avoid interactions with the immune system. In our proposed design, PMPC is coated on the surface of MSN-COOH via the LbL approach, which, with a super-hydrophilic property, can achieve immune escape without being identified by the macrophages. To prove this mechanism, the membrane impermeant nuclear dye, PI, is encapsulated into the nanoparticles. The macrophages are co-cultured with PI-loaded MSN-COOH and PI-loaded MSN-COOH@PMPC for 3 h. Fig. 4a shows that a large amount of PI-loaded MSN-COOH is engulfed by the macrophages. However, after PMPC coating on the surface of nanoparticles, MSN-COOH@PMPC becomes extremely hydrophilic and therefore can hardly be recognized by the macrophages. In the absence of PMPC protection, PI-loaded MSN-COOH is identified and endocytosed by the macrophages. Because PI binds to nucleus, the nucleus of macrophages co-cultured with PI-loaded MSN-COOH are stained to red. The quantitative characterization of the fluorescent images via fluorescence intensity is provided in Supporting Information (Fig. S18). The cellular uptake result indicates that the coating of PMPC on the surface of MSN can effectively improve the bioavailability of the developed drug nanocontainer.

The charged PMPC can bind adjustive water molecules due to ion-dipole interaction, which also enhances the van der Waals force [35]. Meanwhile, the free water molecules nearby further bind or rapidly exchange with the interacted water molecules owing to dipole-dipole interaction, especially hydrogen bonds, to form a hydration layer (Fig. 4b). A significant property of the hydration layer is to achieve improved lubrication [24]. Therefore, the decrease in COF, as a consequent result, can prove the formation of the hydration layer. We measure the COF with or without MSN-COOH@PMPC under a variety of concentrations from 0.025 mg mL^{-1} to 0.1 mg mL^{-1}. The result demonstrates that COF has been reduced at least by half after adding

MSN-COOH@PMPC (Fig. 4c). The formation of the hydration layer is also confirmed by a sharp weight loss of the bound water (under 180 °C) in the TGA curve of MSN-COOH@PMPC. The hydration layer, just like an invisible cloth, holds a much higher hydrophilicity than macrophage for shielding the inner nanoparticles to achieve immune escape.

3.4. Biocompatibility evaluation

Following the analysis of immune escape mechanism, we investigate the biocompatibility of the lubricated nanoparticles via *in vitro* and *in vivo* studies. As a precondition for clinical application, the toxicological tests of MSN-COOH, PMPC, and MSN-COOH@PMPC are first performed with different cell lines. Two cell lines from human liver (QSG-7701 cell line) and kidney (293 cell line) are chosen because liver and kidney are the most critical metabolic organs. Meanwhile, we also include a cancer cell line (Hela), which has been commonly used for the evaluation of biocompatibility. A range of concentrations from 0 to 2 mg mL^{-1} are used for the *in vitro* toxicological test. The result in Fig. S19 shows that all the cells maintain a survival rate of more than 90%, indicating excellent *in vitro* biocompatibility of the materials.

More directly, we also perform *in vivo* toxicological test by characterizing the physiological structure of heart as the M2 receptor is mainly distributed in cardiomyocytes. The tissue slides of heart structure are shown in Fig. 5a. We measure left ventricular long and short axis length and ventricular septal thickness of four different groups including saline, MSN-COOH@PMPC, MCh-loaded MSN-COOH, and MCh-loaded MSN-COOH@PMPC. There are no significant differences in these values for all the groups as shown in Fig. 5b, which indicates that the nanoparticles have good *in vivo* biocompatibility and no great adverse effect on heart structure. Additionally, the arrangement of myocardial sarcomere is closely related to contractile function of cardiomyocytes. Therefore, the Z-line of sarcomere is clearly shown by immunofluorescence staining of α-actinin to examine the arrangement of the sarcomere (Fig. 5c). The sarcomeres of cardiomyocytes in all the groups are regularly arranged, and no obvious disarray is observed, which indicates that the nanoparticles have no significant adverse effect on the arrangement of myofibrils. The evaluation for the proportion of apoptotic cardiomyocytes is shown in Fig. 5d, which is determined by flow cytometry (Fig. 5e). These results indicate that MSN-COOH and MCh-loaded MSN-COOH@PMPC generate no adverse effect on cardiomyocyte apoptosis. Furthermore, the relative protein expression of apoptosis-related proteins (caspase3 and cleaved caspase3) of the primary cardiomyocytes in neonatal mice is examined by western blot (Fig. 5f), and the quantitative analysis in molecular level is shown in Fig. 5g. The result of western blot is consistent with that of flow cytometry, indicating that the nanoparticles have no adverse effect on cardiomyocyte apoptosis.

In addition to the pathological studies on myocardial tissue, we have also investigated the potential side effects of the developed nanoparticles on liver and kidney, which represent two essential metabolic organs in the human body. Toxic nanomedicine can cause a serious burden and even pathological lesion on these organs. Chemical induced liver injury usually appears as necrosis in liver tissue and inflammatory cell infiltration. It is shown in Fig. 6a that all liver tissues keep normal physiological state and no necrosis has been observed after treating with the nanoparticles. Additionally, no obvious inflammatory cell infiltration is detected for all the groups. Generally, drug nephrotoxicity shows as degeneration and necrosis of kidney cells. The result in Fig. 6b
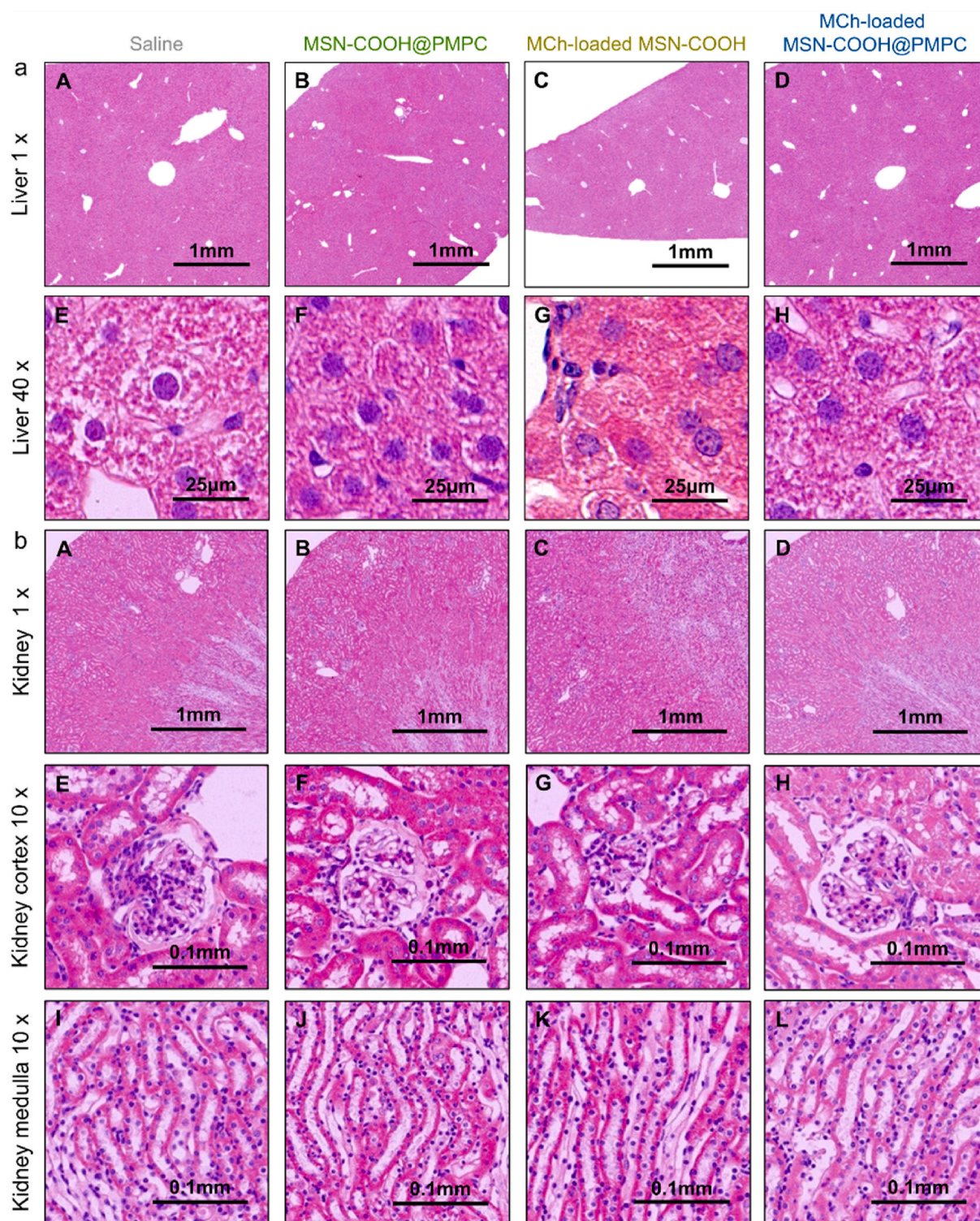
Fig. 6. The *in vivo* biocompatibility of the nanoparticles on **a** liver and **b** kidney in the mice treated with saline, MSN-COOH@PMPC, MCh-loaded MSN-COOH, and MCh-loaded MSN-COOH@PMPC. The images are arranged as follows, liver tissue (line 1), liver cells (line 2), kidney tissue (line 3), kidney cortex (line 4), and kidney medulla (line 5).

demonstrates that the kidney tissues are normal, and there is no necrosis of the kidney cells. Furthermore, the structures of glomeruli and surrounding tubules in the renal cortex are normal, and no cell degeneration and necrosis are detected. The renal medulla area, mainly the distal convoluted tubules and collecting ducts, also shows a normal structure without degeneration and necrosis.

3.5. Bioreceptor recognition

Before the validation of bioreceptor recognition of the developed nanoparticles via *in vivo* test, we analyze the molecular structure of PMPC monomer (MPC), which is similar to that of ACh. We speculate that PMPC may have the performance of M2 receptor recognition as ACh. We first calculate the binding energies of MPC and ACh to M2
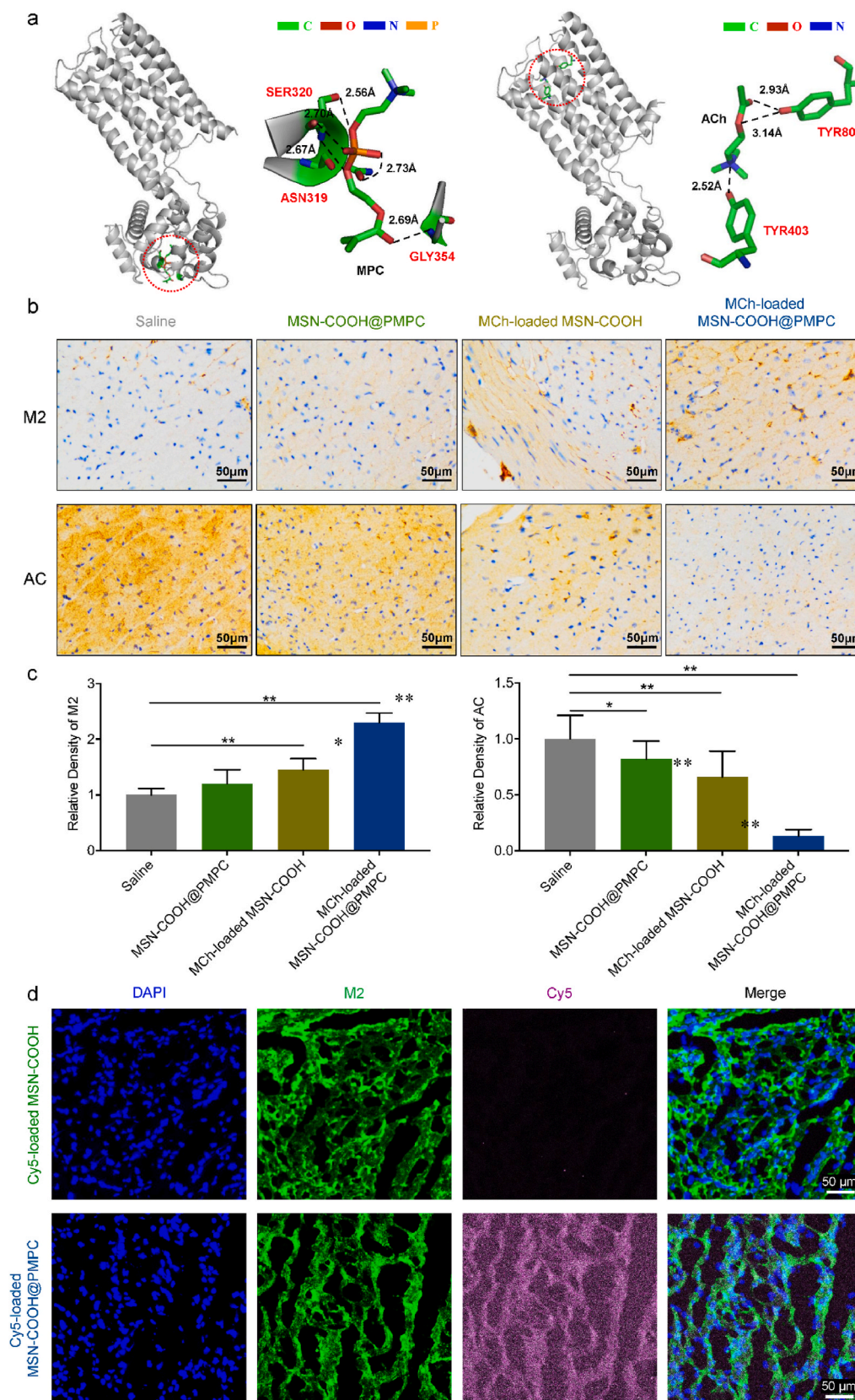
Fig. 7. Bioreceptor recognition validation of the nanoparticles. **a** The 3D structures of M2-MPC and M2-ACh complex predicted by molecular simulation. The enlarged images display the hydrogen bonds between receptor (M2) and ligand (MPC or ACh). The black dotted lines indicate the atom-atom distance. **b** The protein expression of M2 receptor and AC in heart tissue treated with saline, MSN-COOH@PMPC, MCh-loaded MSN-COOH, and MCh-loaded MSN-COOH@PMPC. **c** The quantification analysis of protein expression for M2 receptor and AC in heart tissue. n = 5, *P < 0.05, **P < 0.01. **d** The immunofluorescence staining images of heart tissues treated with Cy5-loaded MSN-COOH and Cy5-loaded MSN-COOH@PMPC.
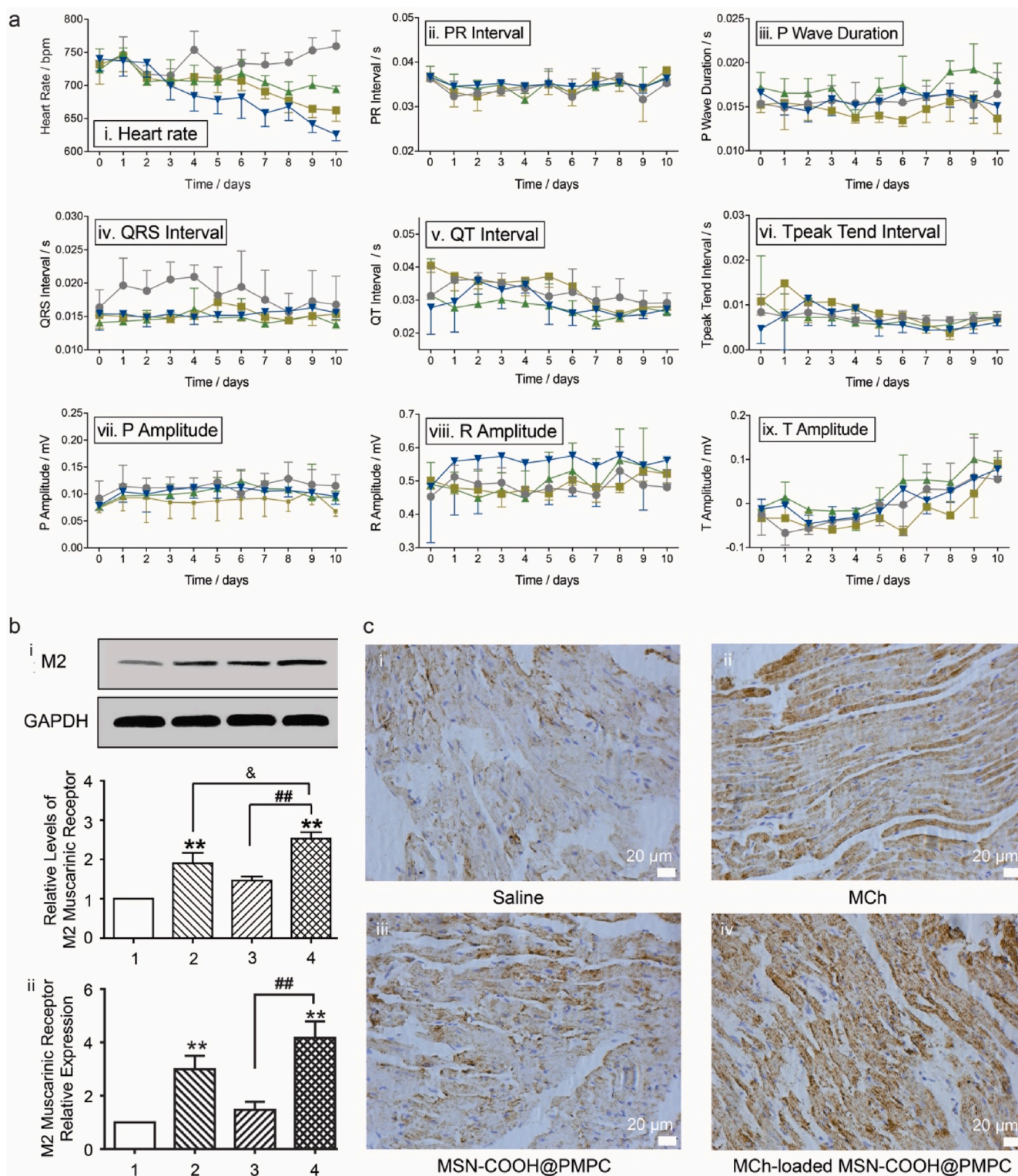
Fig. 8. The *in vivo* study of the nanoparticles. **a** The detection and comparison of ECG in the mice for the first 10 days treated by saline (grey), MSN-COOH@PMPC (green), MCh-loaded MSN-COOH (yellow), and MCh-loaded MSN-COOH@PMPC (blue), n = 15. (i) heart rate; (ii) PR interval; (iii) P wave duration; (iv) QRS interval; (v) QT interval; (vi) T_{peak} tend interval; (vii) P amplitude; (viii) R amplitude; (ix) T amplitude. **b** M2 receptor recognition evaluation in the rats. Male rats are randomly divided into four groups (n = 6): (1) Normal (0.9% saline), (2) MCh, (3) MSN-COOH@PMPC, and (4) MCh-loaded MSN-COOH@PMPC. (i) M2 protein expression levels in rat heart tissues. **P < 0.01 *vs.* group 1; ##P < 0.01 *vs.* group 3; &P < 0.05 *vs.* group 2. (ii) M2 mRNA expression levels in rat heart tissues. **P < 0.01 *vs.* group 1; ##P < 0.01 *vs.* group 3. **c** Immunohistochemical staining of M2 antibody from paraffin-embedded rat heart sections.

receptor using the molecular simulation method. The three-dimensional (3D) structures and interaction energies of M2 with MPC (M2-MPC) and M2 with ACh (M2-ACh) complex are displayed in Fig. 7a and Table S4. It is demonstrated that the total interaction energy of M2-MPC (-1.99 kcal mol^{-1}) and M2-ACh (-5.46 kcal mol^{-1}) complex is comparable, which indicates that MPC has similar binding capability to ACh. As for the M2-MPC complex, hydrogen bond energy predominates among different energies, which promotes the binding between M2 and MPC mainly at three amino acids (SER320, ASN319, and GLY354). Regarding with the M2-ACh complex, Van der Waals energy, hydrogen bond energy, and electrostatic energy all contribute to the binding interactions, and the amino acids of TYR403 and TYR80 in M2 form hydrogen bond with ACh (the other interactions with the atom-atom distance are shown in Supporting Information as Fig. S20). However, because the acetyl moiety (in ACh) is replaced by the phosphate group (in MPC), the bonding energy of MPC is weakened compared with that of ACh.

The recognition of M2 receptor is further confirmed by the *in vitro* cell study (Fig. S21) and a series of *in vivo* tests, which has been observed in both mice and rat (Fig. 7b–d and Fig. 8). In Fig. 7b–c, the protein expression of M2 increases sharply for MCh-loaded MSN-COOH@PMPC compared with MSN-COOH@PMPC and MCh-loaded MSN-COOH, which indicates that the targeting of the nanoparticles via PMPC improves the bioavailability of MCh. It is noted that without MCh loading, MSN-COOH@PMPC still results in a slight increase in protein expression of M2, which is attributed to the similar structure between MPC and MCh. Additionally, the over-expression of M2 greatly suppresses the production of adenylyl cyclase (AC). Therefore, the experimental group treated with MCh-loaded MSN-COOH@PMPC leads to the lowest expression of AC. In Fig. 7d, it is shown from the immunofluorescence staining images that cyanine5 (Cy5)-loaded MSN-COOH@PMPC successfully targets to the heart tissues with M2 receptor, while no obvious targeting effect has been observed for Cy5-loaded MSN-COOH (the experimental procedure of the *in vivo* test is provided in Supporting Information).

In addition to the change in protein expression, the activation of M2 receptor also intuitively affects heart rate. A noticeable decrease in heart rate of mice has been observed after treating with MCh-loaded MSN-COOH@PMPC because the activated M2 can lower the heart rate [36], which further proves the *in vivo* targeting effect of the nanoparticles. ECG, as an approach that can accurately reflects heart rhythm, not only detects the heart rate of mice, but also investigates the risk factors on arrhythmia in detail (Fig. 8a). Except for the saline group, the other groups all display a drop in heart rate. Compared with MSN-COOH@PMPC and MCh-loaded MSN-COOH, the decrease in heart rate for the group of MCh-loaded MSN-COOH@PMPC indicates the greatest inhibition outcome after treatment, as PMPC on the surface of the nanoparticles contributes to both macrophage escape and targeting effect. In addition, the inhibition does not affect the normal functions of the heart and all the durations and intervals have no significant changes, which further proves the low arrhythmia risk of the materials.

To further demonstrate the targeting effect of MSN-COOH@PMPC on M receptor, the M2 expressions of protein and mRNA are collected and analyzed from rat heart tissues. As shown in Fig. 8b, MCh-loaded MSN-COOH@PMPC exhibits a significant increase on the protein expression of M2 compared with that of MCh, which indicates that the developed nanoparticles has good targeting effect to M2. In addition, MSN-COOH@PMPC mildly enhances the protein expression of M2 due to a similar chemical structure to MCh. Similar results are collected from the mRNA expression of M2 by quantitative real-time polymerase chain reaction (PCR, Fig. 8b), thus further confirming the targeting effect of the developed nanoparticles. Fig. 8c shows the representative sections of heart tissues stained with M2 antibody. Clearly, the treatments with both MCh and MCh-loaded MSN-COOH@PMPC significantly enhance M2 expression, and the outcome is more potent for MCh-loaded MSN-COOH@PMPC because of the targeting effect. MSN-COOH@PMPC holds a mild increase in the expression of M2 compared with the normal group, which is attributed to the similar chemical structure of PMPC to MCh.

4. Conclusions

In the present study, PMPC, as a typical polyelectrolyte that can form hydrated layer due to its zwitterionic group, was coated on the surface of drug-loaded MSN by LbL approach. It was found that the hydration layer greatly increased the surface hydrophilicity, which weakened the ability of macrophages to recognize the lubricated nanoparticles, thus achieving the effect of immune escape. In addition, by comparing the chemical structure, we also proposed that the structure of PMPC monomer was similar to that of ACh, which could generate a strong binding with M receptor. Based on the results of both molecular simulation and *in vivo* study, we successfully targeted drug-loaded MSN-COOH@PMPC to M2 receptor-rich heart tissues in both mice and rats. In conclusion, the lubricated nanocontainers developed herein achieved bioreceptor recognition based on macrophage escape and may provide a fundamental basis for the design of related biomaterials.

CRediT authorship contribution statement

Yulong Sun: Investigation, Methodology, Formal analysis, Writing – original draft. **Yanxin Han:** Investigation, Methodology, Formal analysis, Writing – original draft. **Yannong Dou:** Methodology, Formal analysis. **Xinqi Gong:** Methodology, Formal analysis. **Haimang Wang:** Formal analysis. **Xiaoyu Yu:** Methodology. **Qiang Wang:** Methodology. **Yixin Wang:** Methodology. **Yue Dai:** Formal analysis, Resources. **Fangfu Ye:** Resources. **Wei Jin:** Formal analysis, Resources, Funding acquisition. **Hongyu Zhang:** Conceptualization, Resources, Writing – review & editing, Funding acquisition.

Declaration of competing interest

The authors declare no conflict of interest.

Acknowledgements

Appendix A. Supplementary data

Supplementary data to this article can be found online at https://doi.org/10.1016/j.bioactmat.2021.12.035.

References

[1] R.A. Petros, J.M. DeSimone, Strategies in the design of nanoparticles for therapeutic applications, Nat. Rev. Drug Discov. 9 (2010) 615–627.
[2] H.H. Gustafson, D. Holt-Casper, D.W. Grainger, H. Ghandehari, Nanoparticle uptake: the phagocyte problem, Nano Today 10 (2015) 487–510.
[3] T. Malachowski, A. Hassel, Engineering nanoparticles to overcome immunological barriers for enhanced drug delivery, Eng. Regen. 1 (2020) 35–50.
[4] S.Y. Fam, C.F. Chee, C.Y. Yong, K.L. Ho, A.R. Mariatulqabtiah, W.S. Tan, Stealth coating of nanoparticles in drug-delivery systems, Nanomaterials 10 (2020) 787.
[5] Y. Yan, T. Sun, H. Zhang, X. Ji, Y. Sun, X. Zhao, L. Deng, J. Qi, W. Cui, H.A. Santos, H. Zhang, Euryale ferox seed-inspired superlubricated nanoparticles for treatment of osteoarthritis, Adv. Funct. Mater. 29 (2019), 1807559.

[6] X. Huang, X. Teng, D. Chen, F. Tang, J. He, The effect of the shape of mesoporous silica nanoparticles on cellular uptake and cell function, Biomaterials 31 (2010) 438–448.

[7] E.-B. Cho, D.O. Volkov, I. Sokolov, Ultrabright fluorescent silica mesoporous silica nanoparticles: control of particle size and dye loading, Adv. Funct. Mater. 21 (2011) 3129–3135.

[8] Y.L. Sun, Y.W. Yang, D.X. Chen, G. Wang, Y. Zhou, C.Y. Wang, J.F. Stoddart, Mechanized silica nanoparticles based on pillar[5]arenes for on-command cargo release, Small 9 (2013) 3224–3229.

[9] Y.L. Sun, Y. Zhou, Q.L. Li, Y.W. Yang, Enzyme-responsive supramolecular nanovalves crafted by mesoporous silica nanoparticles and choline-sulfonatocalix [4]arene [2]pseudorotaxanes for controlled cargo release, Chem. Commun. 49 (2013) 9033–9035.

[10] H. Li, L.-L. Tan, P. Jia, Q.-L. Li, Y.-L. Sun, J. Zhang, Y.-Q. Ning, J. Yu, Y.-W. Yang, Near-infrared light-responsive supramolecular nanovalve based on mesoporous silica-coated gold nanorods, Chem. Sci. 5 (2014) 2804–2808.

[11] M. Bouchoucha, R.C. Gaudreault, M.-A. Fortin, F. Kleitz, Mesoporous silica nanoparticles: selective surface functionalization for optimal relaxometric and drug loading performances, Adv. Funct. Mater. 24 (2014) 5911–5923.

[12] Z. Li, J.C. Barnes, A. Bosoy, J.F. Stoddart, J.I. Zink, Mesoporous silica nanoparticles in biomedical applications, Chem. Soc. Rev. 41 (2012) 2590–2605.

[13] Y. Sun, Y. Sun, L. Wang, J. Ma, Y.-W. Yang, H. Gao, Nanoassembles constructed from mesoporous silica nanoparticles and surface-coated multilayer polyelectrolytes for controlled drug delivery, Microporous Mesoporous Mater. 185 (2014) 245–253.

[14] Q.L. Li, Y. Sun, Y.L. Sun, J. Wen, Y. Zhou, Q.M. Bing, L.D. Isaacs, Y. Jin, H. Gao, Y. W. Yang, Mesoporous silica nanoparticles coated by layer-by-layer self-assembly using cucurbit[7]uril for in vitro and in vivo anticancer drug release, Chem. Mater. 26 (2014) 6418–6431.

[15] J.L. Paris, M.V. Cabanas, M. Manzano, M. Vallet-Regi, Polymer-grafted mesoporous silica nanoparticles as ultrasound-responsive drug carriers, ACS Nano 9 (2015) 11023–11033.

[16] Y. Sun, H. Zhang, Y. Wang, Y. Wang, Charged polymer brushes-coated mesoporous silica nanoparticles for osteoarthritis therapy: a combination between hydration lubrication and drug delivery, J. Contr. Release 259 (2017) e45–e46.

[17] J. Wen, K. Yang, F. Liu, H. Li, Y. Xu, S. Sun, Diverse gatekeepers for mesoporous silica nanoparticle based drug delivery systems, Chem. Soc. Rev. 46 (2017) 6024–6045.

[18] B.S. Zolnik, A. Gonzalez-Fernandez, N. Sadrieh, M.A. Dobrovolskaia, Nanoparticles and the immune system, Endocrinology 151 (2010) 458–465.

[19] C.D. Walkey, J.B. Olsen, H. Guo, A. Emili, W.C. Chan, Nanoparticle size and surface chemistry determine serum protein adsorption and macrophage uptake, J. Am. Chem. Soc. 134 (2012) 2139–2147.

[20] S.M. Moghimi, Chemical camouflage of nanospheres with a poorly reactive surface: towards development of stealth and target-specific nanocarriers, Biochim. Biophys. Acta 1590 (2002) 131–139.

[21] Y. Zhang, N. Kohler, M. Zhang, Surface modification of superparamagnetic magnetite nanoparticles and their intracellular uptake, Biomaterials 23 (2002) 1553–1561.

[22] J. Klein, Hydration lubrication, Friction 1 (2013) 1–23.

[23] X. Tan, Y. Sun, T. Sun, H. Zhang, Mechanised lubricating silica nanoparticles for on-command cargo release on simulated surfaces of joint cavities, Chem. Commun. 55 (2019) 2593–2596.

[24] Y.X. Wang, Y.L. Sun, Y.H. Gu, H.Y. Zhang, Articular cartilage-inspired surface functionalization for enhanced lubrication, Adv. Mater. Interfac. 6 (2019) 1900180.

[25] C.P. Green, H. Lioe, J.P. Cleveland, R. Proksch, P. Mulvaney, J.E. Sader, Normal and torsional spring constants of atomic force microscope cantilevers, Rev. Sci. Instrum. 75 (2004) 1988–1996.

[26] M. Varenberg, I. Etsion, G. Halperin, An improved wedge calibration method for lateral force in atomic force microscopy, Rev. Sci. Instrum. 74 (2003) 3362–3367.

[27] N. Eswar, B. Webb, M.A. Marti-Renom, M.S. Madhusudhan, D. Eramian, M.-y. Shen, U. Pieper, A. Sali, Comparative protein structure modeling using modeller, Curr. Protoc. Bioinforma. 15 (2006), 5.6.1–5.6.30.

[28] A. Roy, A. Kucukural, Y. Zhang, I-tasser: a unified platform for automated protein structure and function prediction, Nat. Protoc. 5 (2010) 725–738.

[29] S. Pronk, S. Pall, R. Schulz, P. Larsson, P. Bjelkmar, R. Apostolov, M.R. Shirts, J. C. Smith, P.M. Kasson, D. van der Spoel, B. Hess, E. Lindahl, Gromacs 4.5: a high-throughput and highly parallel open source molecular simulation toolkit, Bioinformatics 29 (2013) 845–854.

[30] W.L. Jorgensen, J. Tirado-Rives, The opls [optimized potentials for liquid simulations] potential functions for proteins, energy minimizations for crystals of cyclic peptides and crambin, J. Am. Chem. Soc. 110 (1988) 1657–1666.

[31] X. Gong, P. Wang, F. Yang, S. Chang, B. Liu, H. He, L. Cao, X. Xu, C. Li, W. Chen, C. Wang, Protein-protein docking with binding site patch prediction and network-based terms enhanced combinatorial scoring, Proteins Struct. Funct. Bioinforma. 78 (2010) 3150–3155.

[32] L.Y. Han, H.H. Lin, Z.R. Li, C.J. Zheng, Z.W. Cao, B. Xie, Y.Z. Chen, Pearls: program for energetic analysis of receptor-ligand system, J. Chem. Inf. Model. 46 (2006) 445–450.

[33] D. Zhao, Q. Huo, J. Feng, B.F. Chmelka, G.D. Stucky, Nonionic triblock and star diblock copolymer and oligomeric surfactant syntheses of highly ordered, hydrothermally stable, mesoporous silica structures, J. Am. Chem. Soc. 120 (1998) 6024–6036.

[34] H.L. Herd, K.T. Bartlett, J.A. Gustafson, L.D. McGill, H. Ghandehari, Macrophage silica nanoparticle response is phenotypically dependent, Biomaterials 53 (2015) 574–582.

[35] U. Raviv, S. Giasson, N. Kampf, J.F. Gohy, R. Jerome, J. Klein, Lubrication by charged polymers, Nature 425 (2003) 163–165.

[36] M.P. Caulfield, Muscarinic receptors-characterization, coupling and function, Pharmacol. Ther. 58 (1993) 319–379.